Quantitative phase imaging with a compact meta-microscope

Check for updates

Junyi Wang[1,2], Rongtao Yu[1,2], Xin Ye[1,2], Jiacheng Sun[1], Jian Li[1], Chunyu Huang[1], Xingjian Xiao[1], Jitao Ji[1], Wenjing Shen[1], Zuoxiu Tie[1], Chen Chen[1] ✉, Shining Zhu[1] & Tao Li[1] ✉

Quantitative phase imaging (QPI) based on the transport-of-intensity equation (TIE) is a powerful technique in label-free microscopy. The image stack required for a successful TIE-QPI is traditionally obtained by translating the object or image plane, and the optical elements used in the conventional TIE-QPI systems are usually bulky and cumbersome. Stable and compact TIE-QPI methods capable of non-motion optical zooming can significantly facilitate applications that demand portability. Here, we propose a non-motion TIE-QPI method based on a dispersive metalens. The dispersive nature of the metalens is utilized to provide a spectral focal tuning. With fixed object and image planes, seven through-focus intensity images are captured by changing the illumination wavelength. The QPI performance is validated by retrieving the surface phase profiles of a microlens array and a phase resolution target, showing a high phase detection accuracy (deviation less than 0.03 wavelength). Subsequently, we established a compact meta-microscope by integrating the metalens with a commercially available CMOS image sensor, which shows good performance in microscopic imaging of unstained bio-samples. Our approach, based on the large-dispersive metalens, facilitates a compact and robust QPI system for optical metrology and label-free microscopy.

Traditional bright-field microscopes mainly utilize opaque specimens to provide sufficient contrast for observation. For near-transparent samples with little contrast, like bio-cells and tissues, fluorescence or staining methods are widely used to enhance intensity contrast. However, exogenous fluorescent agents or staining labels may be toxic to living cells[1,2]. Label-free microscopy, serving as a complementary technique to fluorescence or staining methods, can provide low phototoxicity and does not demand sophisticated sample preparation procedures. It transfers the intrinsic phase information of the intensity-transparent samples into intensity contrast. Typical examples of label-free microscopy are Zernike phase contrast microscopy[3] (ZPC) and differential interference contrast microscopy[4] (DIC). However, they provide only qualitative visualization instead of quantitative mapping of the phase profile.

Quantitative phase imaging (QPI) techniques, such as digital holographic microscopy[5], Fourier ptychographic microscopy[6], quantitative differential phase contrast microscopy[7,8], transport-of-intensity equation (TIE)[9–11], have proven to be powerful tools in label-free microscopy[12], and have witnessed rapid development in recent decades. The images provided by QPI, unlike ZPC or DIC outputs, can be put to automated analysis like

cell segmentation[13], facilitating research on cell structures, cell dynamics, and the calculation of cell mass and volume, etc. Among diverse QPI methods, TIE is non-interferometric and highly compatible with conventional microscope setups with Köhler illumination. It requires only multiple intensity measurements from axially displaced planes for deterministic phase retrieval. TIE-QPI methods have found great potential in biomedical and metrological applications[14,15]. Nevertheless, traditional TIE-QPI methods[14–19], mechanical scanning required or not, are all based on conventional bulky optical elements and demand careful adjustments of optical setups. This is unfavorable in applications that call for compactness and portability, such as point-of-care testing.

Imaging system miniaturization has advanced rapidly in past years, bringing about technological developments like miniaturized fluorescence microscopes[20,21], lensless microscopy[22–24], chip-scale metalens microscopes[25,26], etc. Among these, metasurface or metalenses, with flat and ultrathin architectures composed of subwavelength units[27,28], have shown massive potential in providing miniaturized solutions for diverse information processing[29–32] or imaging applications[33,34], like fluorescence imaging[35,36], polarization imaging[37], ultraspectral imaging[38], phase imaging[39–45],

[1]National Laboratory of Solid State Microstructures, Key Laboratory of Intelligent Optical Sensing and Manipulation, Jiangsu Key Laboratory of Artificial Functional Materials, College of Engineering and Applied Sciences, Nanjing University, Nanjing 210093, China. [2]These authors contributed equally: Junyi Wang, Rongtao Yu, Xin Ye. ✉e-mail: chenchen2021@nju.edu.cn; taoli@nju.edu.cn

tomographic imaging[46,47], multimode imaging[48], wide-angle imaging[49], etc. Current metasurface-based QPI or quantitative phase gradient imaging (QPGI) methods either require two cascaded metasurfaces[40], or place the metasurface at the Fourier plane, both of which complicate the entire system[39,45]. Therefore, a QPI method composed of a single-layered metalens in a fixed system free of complicated configurations is highly desirable.

In this article, we propose and experimentally demonstrate a dispersive metalens based TIE method to realize QPI without mechanically translating the image or object plane. We exploit the dispersive nature of metalenses, which can introduce spectral dispersion large enough to provide evident focal length deviations, thereby enabling non-mechanical optical zooming. Specifically, by sweeping the illumination wavelength while fixing the image and object planes, we obtain a stack of through-focus intensity images bound for a multi-plane TIE phase recovery method[18,19] to retrieve the in-focus phase information. The QPI performance of the proposed method is characterized on a commercial microlens array, showing the phase deviation is less than 0.03 wavelength (i.e., 0.1 rad by calculation) as compared with the atomic force microscope (AFM) measured surface profile. Its powerful capability in phase measurement on the near-transparent samples is further validated on a phase resolution target. Moreover, the dispersive metalens based TIE method, free of mechanical translation of the image or object plane, enables the direct integration of the metalens with a commercial image sensor to establish a meta-microscope. The size of the meta-microscope is $36 \times 36 \times 14$ mm^3, which is much smaller than the conventional imaging objectives and also achieves a relatively higher level of miniaturization than several lensless microscopy methods[23,24]. The QPI performance of the meta-microscope is tested on unstained bio-samples, also showing good results.

Results

Concept of the metalens-based QPI

The quantitative relationship between the axial intensity derivative and the phase of the transverse optical field was first derived by Teague in a second-order elliptic partial differential equation, later termed TIE, which is written as

$$-k\frac{\partial I(x,y)}{\partial z} = \nabla_\perp \cdot [I(x,y)\nabla_\perp \varphi(x,y)] \tag{1}$$

where k is the wavenumber $2\pi/\lambda$, λ is the wavelength, z is the coordinate along the optical axis, I and φ are the intensity and phase distributions at the recorded plane (generally the focal plane), and $\nabla_\perp$ is the two-dimensional gradient operator over the transverse coordinates x and y. When satisfying certain boundary conditions, the absolute phase can be deterministically retrieved without phase unwrapping or iterative approximations. Due to the convenience of being non-interferometric and highly compatible with basic microscope setups, TIE is chosen as the phase solver to achieve a metalens-based QPI. According to the working principle of TIE, a precise axial intensity derivative is necessary, which can be approximately obtained with different methods. The most straightforward approach is to use the difference between two intensity images. However, the result is usually sensitive to the choice of defocus distance in practical experiments. In comparison, acquiring multiple through-focus images[18,19] can provide a more robust approximation of the axial intensity derivative (see Supplementary Note 1 for details about the multi-plane methods). The image stack is traditionally acquired by mechanically scanning the object plane (or the conjugate image plane), undoubtedly involving complicated mechanical elements. Inspired by the large dispersive nature of metalenses, which has been used to access a microscope tomography[46], we conceived the concept of non-motion scanning using a dispersive metalens, as schematically shown in Fig. 1. In this case, the TIE should be converted to a more general form[50] as

$$-2\pi\frac{\partial I(x,y)}{\partial \xi} = \nabla_\perp \cdot [I(x,y)\nabla_\perp \varphi(x,y)] \tag{2}$$

where $\xi = \lambda z$ represents the general defocus distance, and the TIE-solving process remains similar. The dispersive nature of metalenses allows optical zooming to capture multiple through-focus images with much smaller wavelength alterations than their refractive counterparts[50]. In the experiment, we captured seven images with varied defocus distances while changing the illumination wavelength from 420 to 480 nm with a 10-nm-interval (the center wavelength λ_0 is 450 nm). The small wavelength sweeping range makes it possible to use a single light-emitting diode (LED, GCI-060404, Daheng Optics Co. Ltd., China) as the light source, accompanied by filters of 10-nm bandwidth (hard-coated bandpass filters from Thorlabs, Inc.). Considering the non-motion optical zooming and the compactness of the single-layered metalens and the LED light source, our dispersive metalens based QPI method shows great prospects in a miniaturized and stable platform.

Fig. 1 | Schematics of the dispersive metalens based QPI. The focal length of the metalens shifts with the sweep of illumination wavelength. When the object and image planes are fixed, multiple defocused images with certain defocused distances can be captured for further TIE phase retrieval. **a**, **b** Illustrations of the approximated axial intensity derivative and retrieved phase from the captured image stack.
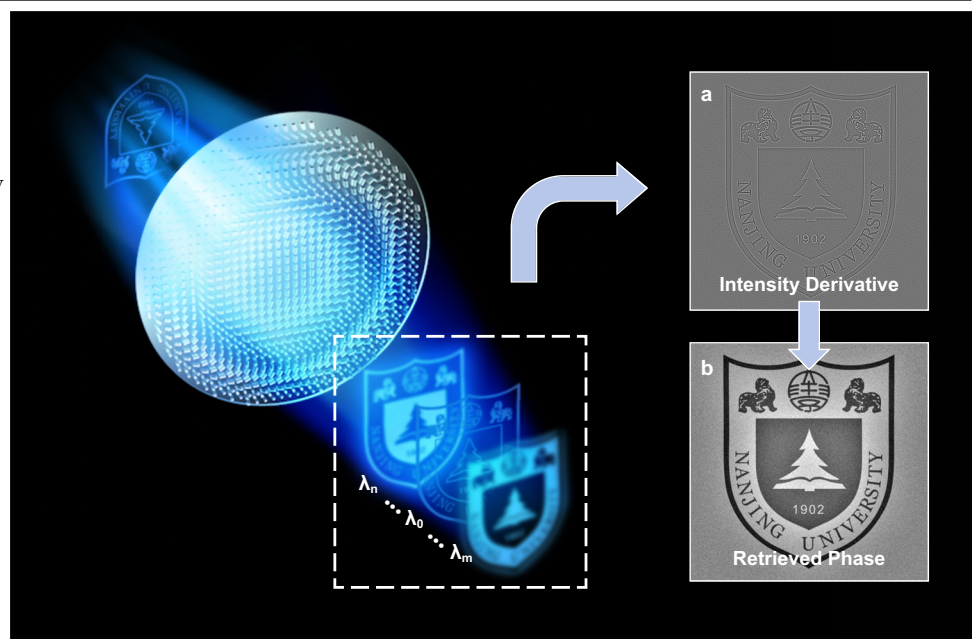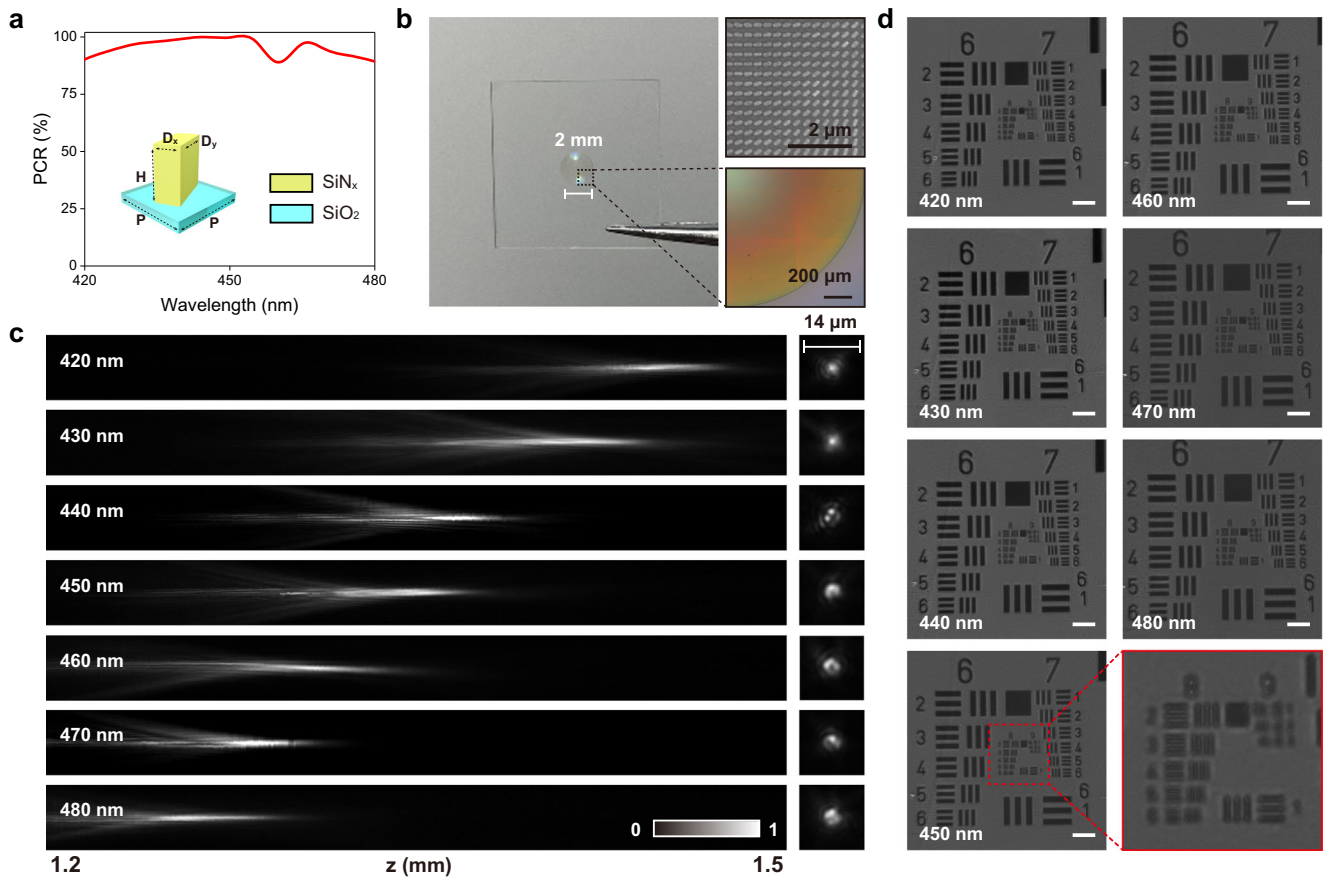
Fig. 2 | Characterization of the fabricated metalens. a Calculated polarization conversion ratio (PCR) of the selected nanofin ($H = 1000$ nm, $Dx = 90$ nm, $Dy = 215$ nm, $P = 300$ nm) in the working wavelength range. The PCR at $\lambda_0 = 450$ nm is 99.89%, and the average one is 95%. **b** Photograph of the fabricated metalens with NA = 0.58 and the diameter $D = 2$ mm. Optical and SEM images are displayed alongside. **c** Measured intensity distributions of the longitudinal light-field cross-sections at targeted wavelengths. The intensity profiles of the respective focal spots are displayed in the right column. **d** Raw images of the 1951 USAF resolution chart captured when the illumination wavelength is changed from 420 to 480 nm. The image distance is fixed for an imaging magnification of 4 at $\lambda_0 = 450$ nm, and the object distance is altered accordingly for in-focus capture. The magnified detail of the image taken at $\lambda_0 = 450$ nm shows that group 8 element 5 (1.23 μm half-pitch resolution) can be distinguished. Scale bar: 15 μm.

Design and Characterization of the metalens

The capability of defocus to transfer phase into intensity variations stems from the imaginary part introduced to the coherent transfer function of the imaging system, as do most optical aberrations. If we assume the phase of a metalens is introduced by the Pancharatnam-Berry (PB) phase and takes the normally used hyperbolic form as

$$\varphi_{hyperbolic} = -\frac{2\pi}{\lambda_0}\left(\sqrt{f^2 + r^2} - f\right) \tag{3}$$

where f is the focal length at λ_0, and r is the radial position, it will induce considerable spherical aberration when the wavelength deviates from λ_0, and it is not suitable for microscopic imaging applications (see Supplementary Note 2 for detailed discussion). To deliver an accurate phase retrieval, it is important to alleviate the influence of unwanted aberrations. Under the microscopic imaging setup, it is proven that the spherical aberration can be significantly reduced, and the field of view (FoV) can be increased by using an aplanatic phase profile[46,48]. The aplanatic phase is deduced as a function of the object distance based on the generalized law of refraction, written as

$$\varphi_{aplanatic} = -\frac{2\pi}{\lambda_0}\left[\sqrt{s^2 + r^2} + \sqrt{\left(\frac{sf}{f - s}\right)^2 + r^2}\right] \tag{4}$$

where s is the object distance. Doublet design methods[51] can also be further utilized to correct off-axis aberrations. The aplanatic phase profile is delivered based on the PB phase method via distributing SiN_x nanofins (height $H = 1000$ nm, length $Dx = 90$ nm, width $Dy = 215$ nm) in a rectangle lattice (lattice period $P = 300$ nm, meeting the Nyquist sampling criterion) on a SiO_2 substrate. Figure 2a depicts that the selected nanofin possesses high polarization conversion ratio (PCR) across the targeted spectrum (see "Methods" for the simulation details). The average PCR is 95%. Figure 2b demonstrates the photograph of the fabricated metalens with a diameter $D = 2$ mm and the optical and scanning electron microscope (SEM) images (see "Methods" for the fabrication details). The numerical aperture (NA) of the metalens was set as 0.58 at $\lambda_0 = 450$ nm (the corresponding ideal focal length is 1.4 mm), and the metalens was designed with an imaging magnification of 4 at $\lambda_0 = 450$ nm.

Figure 2c demonstrates apparent focal shifts with different illumination wavelengths. The imaging performance of the metalens is good according to the captured images of the 1951 United States Air Force (USAF) resolution test chart shown in Fig. 2d. The measured intensity distributions of longitudinal cross-sections of the optical field are obtained with normally incident light. This is unsuitable for determining the actual defocus distances at different wavelengths because the aplanatic phase is designed under the illumination of an on-axis point source with a small object distance. When the image distance is set, the exact defocus distances from spectral zooming can be obtained through refocusing experiments shown in Fig. 2d. The defocus distance equals the negative number of the
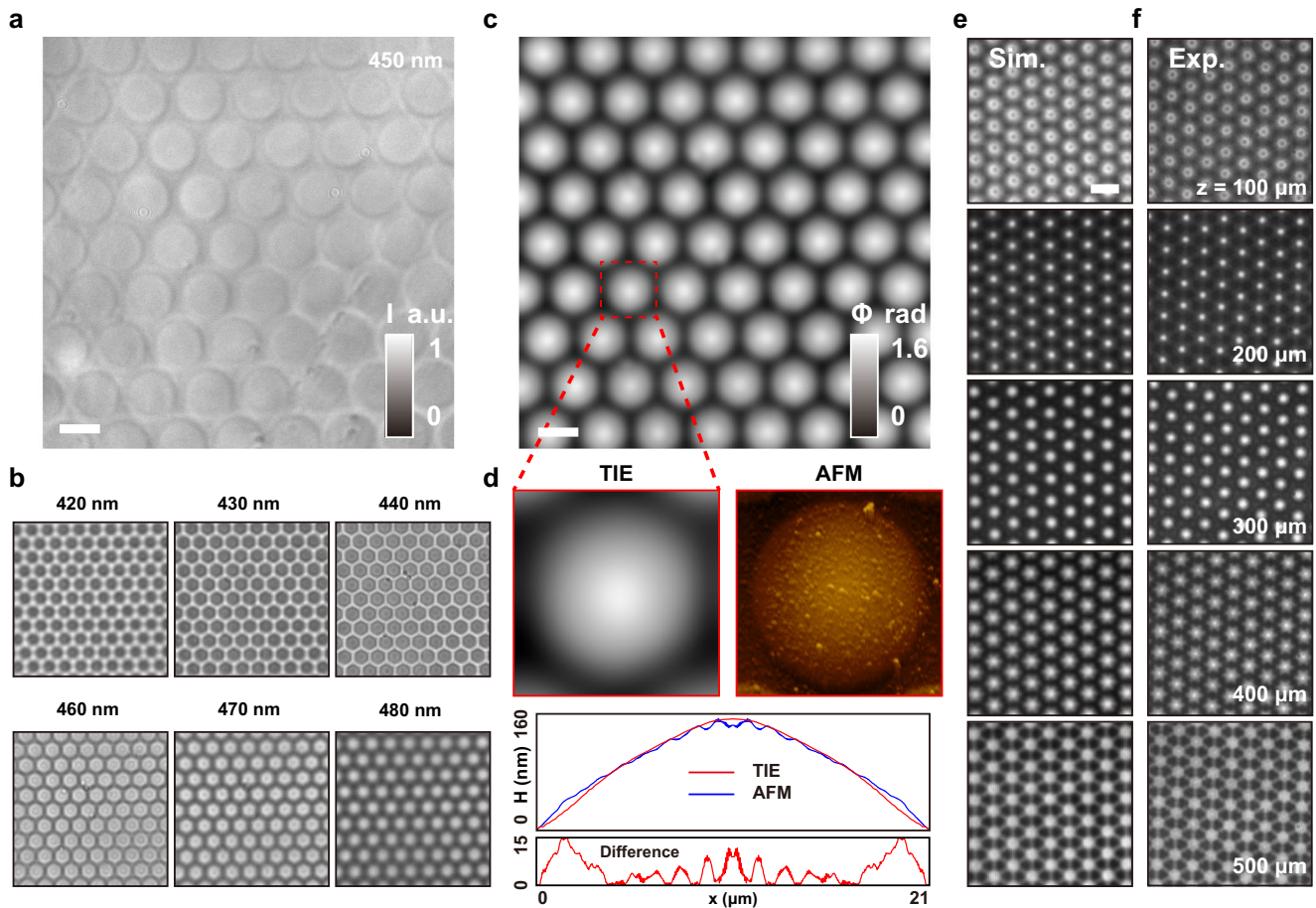
Fig. 3 | Quantitative phase imaging of a microlens array to validate the phase retrieval accuracy. a In-focus image of the microlens array surface captured by the metalens at $\lambda_0 = 450$ nm. The imaging magnification is set as 4. **b** Defocused images captured by the metalens with illumination wavelengths from 420 to 480 nm. **c** Reconstructed in-focus phase profile of the microlens array. **d** Enlarged red-dashed box region of one microlens and AFM image of one microlens. The radial averages of the respective surface profiles and the profile difference curve are depicted below. **e, f** Comparison between the simulated and the experimentally measured transverse intensity distributions of the optical field transmitted through the microlens array with a distance of 100–500 µm with a 100-µm-interval. The imaging magnification of the field measurement system was adjusted to be approximately the same as the reconstructed field. Scale bars in **a**, **c**, and **e**, **f** are 20 µm.

refocusing distance when the illumination wavelength deviates from $\lambda_0 = 450$ nm. The defocus distances are measured as -172 µm, -111, -55, 0, 52, 101, and 147 µm for illumination wavelengths ranging from 420 to 480 nm with a 10-nm-interval. The measured seven defocus distances show good accordance with the theoretically predicted ones following the equation as

$$z_{defocus} = s_0 - \sqrt{\left\{ r_p / \left[\frac{\lambda}{\lambda_0} \left(\frac{r_p}{\sqrt{r_p^2 + s_0^2}} + \frac{r_p}{\sqrt{r_p^2 + s_0'^2}} \right) \right] - \frac{r_p}{\sqrt{r_p^2 + s_0'^2}} \right\}^2 - r_p^2} \tag{5}$$

when the r_p is set as half of the radius of the metalens. The s_0 and s_0' represent the object and image distance at the center wavelength. The details and illustrations of the experimental setups to measure the chromatic dispersion and imaging performance can be found in "Methods" and Supplementary Fig. S2.

QPI performance

We first characterized the QPI capability of the dispersive metalens based system using a commercial microlens array made of fused silica (pitch = 21 µm, $f = 500$ µm, sublenses are plane-convex lenses, refractive index is 1.47). The experimental setup is the same as used in the imaging performance characterization above. In the imaging experiment, we fixed the image and object distances the same as the ones at $\lambda_0 = 450$ nm. The magnification of the singlet imaging system inevitably changes with the wavelength-switching induced focal shifts. The magnification at each wavelength is calibrated as 3.64, 3.76, 3.89, 4, 4.12, 4.24, and 4.37, respectively. Although the aplanatic phase of the metalens was designed for imaging magnification of 4, the change of magnification only brings marginal spherical aberrations, which will not significantly influence the phase retrieval (see Supplementary Note 2 for detailed discussion).

The image stack of the microlens array captured by the dispersive metalens is shown in Fig. 3a, b. The magnification and defocus effects can be easily observed, which validates the design concept. Before the phase retrieval, we rescaled the captured images with respect to the one with the lowest imaging magnification. The scaling process is carried out in the frequency domain to avoid undesired scaling errors in the real space. The cut-off frequency of the intensity spatial spectrum will increase with magnification. Thus, we cut out the spectrum range for all images to match that of the image shot at $\lambda = 420$ nm, which has the lowest cut-off frequency. Afterwards, inverse Fourier transformation is employed to get rescaled real-space images, and the missing pixels at the edge of the images were made up with zero. Then, the axial intensity derivative is obtained from the seven through-focus images with precision to the sixth order. The retrieved in-focus phase at $\lambda_0 = 450$ nm is demonstrated in Fig. 3c. The cross-sectional phase profile (radial average) of a single microlens indicated by the red-dashed box shows good accordance with the surface profile measured by AFM, as is shown in Fig. 3d, and the profile difference is less than 15 nm
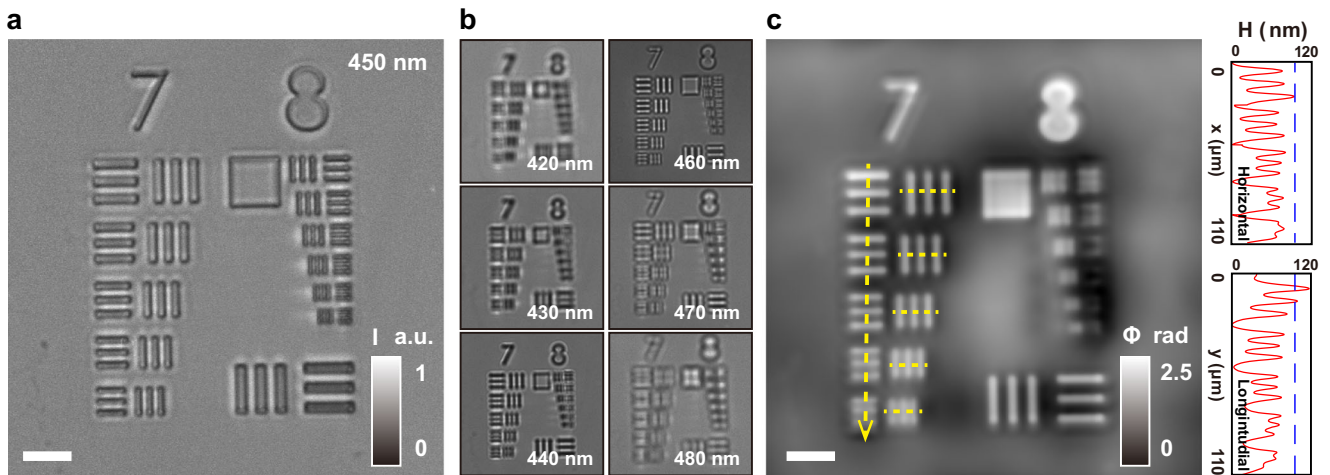
Fig. 4 | Quantitative phase imaging of a homemade phase resolution target to evaluate the phase recovery resolution. a In-focus image of the phase resolution target captured by the metalens at $\lambda_0 = 450$ nm. The imaging magnification is set as 4. Due to the scattering of the edges of resolution target elements, the structures are more obvious than the microlens array. **b** Defocused images captured by the metalens with varied illumination wavelengths. **c** Reconstructed in-focus phase profile of the phase resolution target. The insets to the right depict the surface profile along the horizontal and longitudinal cutlines indicated by the yellow-dashed lines. Scale bars in **a** and **c** are 8 μm.
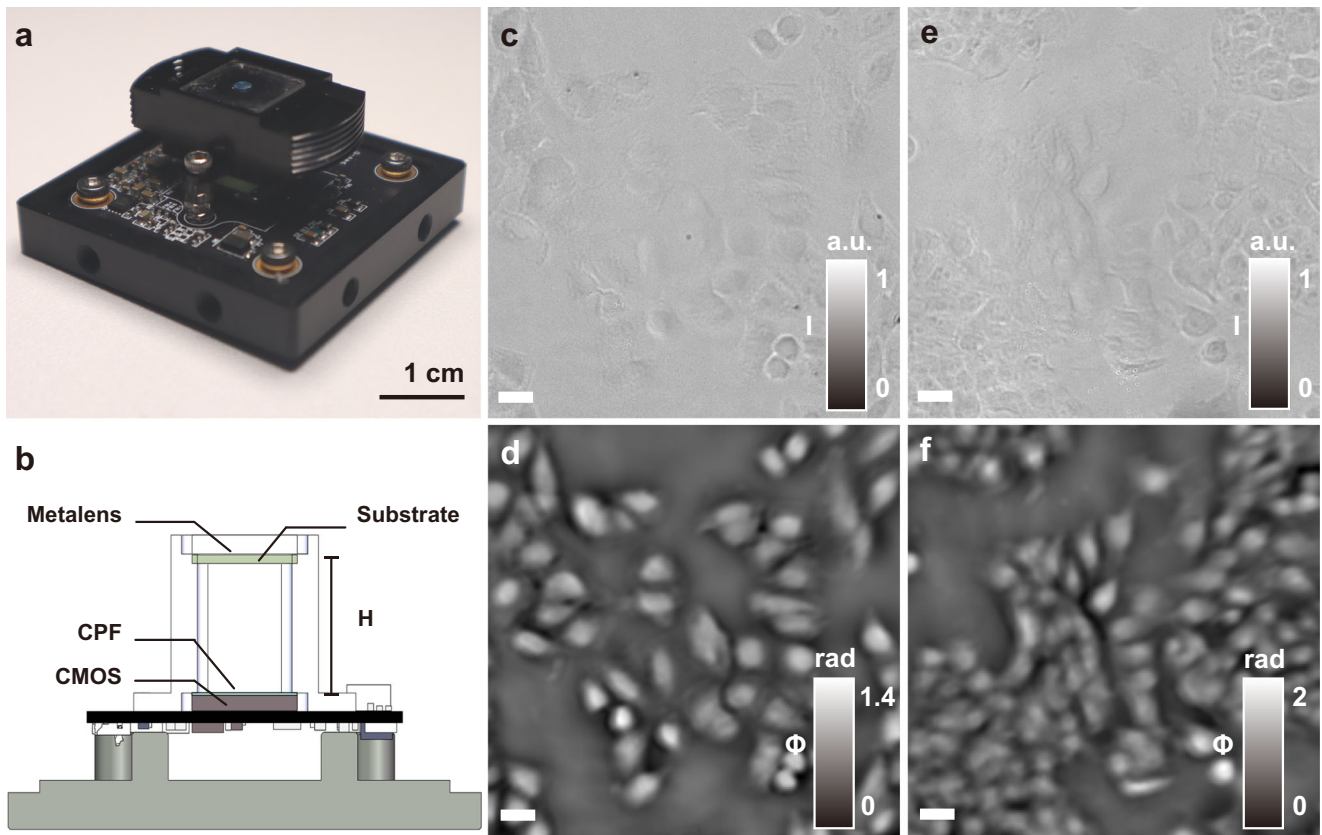

Fig. 5 | Quantitative phase imaging of unstained bio-samples with the meta-microscope. a Photograph of the meta-microscope (length: 36 mm, width: 36 mm, and height: 14 mm). **b** Schematic illustration of the meta-microscope with the distance between the metalens surface and the CMOS as $H = 7$ mm, resulting an imaging magnification of 4. CPF represents circularly polarized film. **c, e** In-focus images of HeLa and 4T1 cells captured by the meta-microscope at $\lambda_0 = 450$ nm. **d, f** Reconstructed in-focus phase profiles of the corresponding cells from the image stack obtained by the meta-microscope. Scale bars in **c–f** are 20 μm.

(approximately $0.03\lambda_0$, i.e., 0.1 rad by calculation). We then utilized the angular spectrum method[52] to numerically calculate the field distribution transmitted through the microlens array with a distance of 100–500 μm with an interval of 100 μm. The calculated results agree well with the measured field distributions as depicted in Fig. 3e, f.

To further verify the QPI capability of our method, we fabricated a phase resolution target with sharp surface profile gradients using SiN_x based on the same fabrication method used on the metasurface (see "Methods" for the fabrication details). The thickness of the sample was measured by a stylus profilometer (KLA, Tencor P-7) to be 100 nm ± 10 nm. The sizes of

the line pairs are set to match group 7 and group 8 of the 1951 USAF resolution test chart. Figure 4a, b shows the captured image stack, and Fig. 4c depicts the reconstructed surface phase profile at $\lambda_0 = 450$ nm. The horizontal and longitudinal cutlines of the surface profile of group 7 indicated by the yellow dashed lines are shown in the inset of Fig. 4c, where the blue dashed line indicates the thickness of 100 nm. The feature size of group 7 element 5 (2.46 μm half-pitch resolution) can be resolved in the reconstructed phase image, as is shown in the inset. The performance of phase resolution is less than the intensity image because the smallest defocus distance here is approximately 50 μm, which is too large to transfer the high-frequency phase information completely. The smallest defocus distance here is limited by the bandwidth of the filter, which would be possibly improved by alternating filters.

After validating the accuracy of our QPI method, we integrated the metalens on a CMOS chip (Imaging source: DMM 27UJ003-ML, pixel size: 1.67 μm × 1.67 μm) to establish a meta-microscope, demonstrating its potential in system miniaturization, as is shown in Fig. 5a, b. We tested the QPI performance of the integrated system on unstained bio-samples (HeLa and 4T1 cells). Figure 5c, e shows the in-focus images obtained by the metalens at $\lambda_0 = 450$ nm (the other through-focus images of the two cells can be found in Supplementary Fig. S3). The image acquisition time for the total 7 captures took about 212 ms. The intensity images can hardly distinguish details due to the low image contrast. By comparison, the reconstructed phase profiles shown in Fig. 5d, f clearly display the structure features, like the cell size, thickness, etc., which could facilitate structure analysis and medical diagnosis. In addition, the quantitative phase information is directly related to the 'dry mass' density map of the cellular structure[12,53] making it convenient for further medical research.

Discussion

In this article, we have proposed and experimentally demonstrated the proof-of-concept of a compact QPI microscope composed of a single-layered dispersive metalens. The large spectral dispersion of the metalens makes the non-motion optical zooming possible simply by sweeping the illumination wavelength. This enables the direct integration of the metalens with a commercially available CMOS image sensor, which demonstrates the prospect of developing a compact and stable platform for a miniaturized QPI system. The QPI results of the microlens array and phase resolution target validate the reconstruction reliability of our method. The QPI images of the unstained bio-samples, which are reconstructed from raw images captured by the meta-microscope, display distinct image contrast, proving the feasibility of our method for biological applications. We envision that the dispersive metalens based QPI will cast new light on the development of miniaturized QPI systems and facilitate applications like point-of-care testing, industrial measurements, etc.

Methods
Simulations

We conducted the full-wave simulation using a commercial finite-difference time-domain (FDTD) solver (Lumerical, Ansys). The refractive indices of SiN_x are 2.0908, 2.0824, 2.0746, 2.0673, 2.0606, 2.0544, and 2.0486 at $\lambda = 420$ nm, 430 nm, 440 nm, 450 nm, 460 nm, 470 nm, and 480 nm. The refractive indices of SiO_2 are 1.4748, 1.4738, 1.4728, 1.4720, 1.4711, 1.4703, and 1.4696 accordingly. The wavelength-dependent refractive indices were measured using a spectroscopic ellipsometer (J.A.Woollam, RC2). Periodic boundary condition was used in the simulation for calculating the polarization conversion ratio. The SiN_x nanofins were set as 1000 nm tall with a rectangle lattice period of 300 nm. The length Dx and width Dy were set to range from 80 nm to 250 nm with a 5-nm-interval. Simulation results of the transmittance and phase modulations of x and y polarized light as a function of Dx and Dy at $\lambda_0 = 450$ nm are presented in Supplementary Fig. S4.

Metasurface and phase resolution target fabrication

The SiNx layer was deposited on a 500-μm-thick fused silica substrate by plasma-enhanced chemical vapor deposition at 300 °C to a final thickness of 1 μm for the metasurface. Then, a positive electron beam resist (200 nm, PMMA A4) was spin-coated onto the substrate and baked at 170 °C for 5 min. Next, a 100-nm-thick layer of a water-soluble conductive polymer (AR-PC 5090) was spin-coated on the resist for the dissipation of electron beam charges. The metalens pattern was written on an electron beam resist using electron beam lithography (EBL, ELS-F125, Elionix). The conductive polymer was then dissolved in water, and the resist was developed in a resist developer solution. Then, the pattern was transferred into a 40-nm-thick chromium layer deposited by electron beam evaporation (EBE) using the lift-off technique. The pattern chromium served as a hard mask for the dry etching of the SiNx layer in a mixture of CHF_3 and SF_6 plasma (Oxford Instruments, PlasmaPro100 Cobra300). The flow rates of the two gases were 60 sccm:6 sccm. Finally, the chromium mask was removed using a solution of ammonium cerium nitrate. The fabrication procedure for the phase resolution target was identical to the one above with one difference in the thickness of the SiN_x layer being 100 nm.

Experimental setup

The schematic of chromatic dispersion characterization is shown in Supplementary Fig. S2. A white-light laser (Fianium Super-continuum, 4 W), accompanied by filters of 10 nm bandwidth, was used for incidence. A left circularly polarized (LCP) film (#88-084, Edmund Optics) was inserted after the source to confirm the incident polarization state. The metalens was mounted on a translation stage. A custom-built microscope consisted of an objective lens (Mitutoyo, NA = 0.42, 20X) and a tube lens (Jcoptix, OLD2466-T2M, $f = 20$ cm) was used to relay the light focused by the metalens to a CMOS image sensor (FLIR, BFS-U3-200S6C-C, pixel size: 2.4 μm × 2.4 μm). A right circularly polarized film (#11-047, Edmund Optics) was inserted between the objective lens and the tube lens to filter the background signals.

The imaging performance of the metalens was characterized using the setups shown schematically in Supplementary Fig. S2. A blue LED (GCI-060404, Daheng Optics Co. Ltd., China) was chosen as light source, and filters of 10 nm bandwidth were utilized to tune the incident wavelength. A $4f$ system with a magnification of 2.7 was utilized to relay the source to the aperture stop. Another $4f$ system with a magnification of 1/3 relayed the field stop onto the object plane. The two $4f$ systems together formed a Köhler illumination system to provide uniform illumination. The metalens and imaging samples were mounted on separate translation stages. The images formed by the metalens were relayed to the same CMOS image sensor by a custom-built microscope consisting of an objective lens (Mitutoyo, NA = 0.28, 10X) and a tube lens (Jcoptix, OLD2466-T2M, $f = 20$ cm). The same pair of orthogonal circularly polarized films used in the chromatic dispersion characterization were inserted after the source and before the tube lens functioning as the polarizer and corresponding analyzer.

Data availability

The datasets used and analyzed during the current study are available from the corresponding author on reasonable request.

References

1. Alford, R. et al. Toxicity of organic fluorophores used in molecular imaging: literature review. *Mol Imaging* **8**, 7290.2009.00031 (2009).
2. Icha, J., Weber, M., Waters, J. C. & Norden, C. Phototoxicity in live fluorescence microscopy, and how to avoid it. *BioEssays* **39**, 1700003 (2017).
3. Zernike, F. Phase contrast, a new method for the microscopic observation of transparent objects part II. *Physica* **9**, 974–986 (1942).
4. Lang, W. *Nomarski Diferential Interference-Contrast Microscopy* (Carl Zeiss Oberkochen, 1982).

5. Marquet, P. et al. Digital holographic microscopy: a noninvasive contrast imaging technique allowing quantitative visualization of living cells with subwavelength axial accuracy. *Opt Lett* **30**, 468–470 (2005).

6. Zheng, G., Horstmeyer, R. & Yang, C. Wide-field, high-resolution Fourier ptychographic microscopy. *Nat. Photonics* **7**, 739–745 (2013).

7. Mehta, S. B. & Sheppard, C. J. R. Quantitative phase-gradient imaging at high resolution with asymmetric illumination-based differential phase contrast. *Opt. Lett.* **34**, 1924–1926 (2009).

8. Tian, L. & Waller, L. Quantitative differential phase contrast imaging in an LED array microscope. *Opt. Express* **23**, 11394 (2015).

9. Teague, M. R. Deterministic phase retrieval: a Green's function solution. *J. Opt. Soc. Am.* **73**, 1434–1441 (1983).

10. Zuo, C. et al. Transport of intensity equation: a tutorial. *Opt. Lasers Eng.* **135**, 106187 (2020).

11. Teague, M. R. Irradiance moments: their propagation and use for unique retrieval of phase. *J. Opt. Soc. Am.* **72**, 1199–1209 (1982).

12. Park, Y., Depeursinge, C. & Popescu, G. Quantitative phase imaging in biomedicine. *Nat. Photonics* **12**, 578–589 (2018).

13. Tian, L. et al. Computational illumination for high-speed in vitro Fourier ptychographic microscopy. *Optica* **2**, 904 (2015).

14. Zuo, C., Chen, Q., Li, H., Qu, W. & Asundi, A. Boundary-artifact-free phase retrieval with the transport of intensity equation II: applications to microlens characterization. *Opt. Express* **22**, 18310 (2014).

15. Zuo, C. et al. High-resolution transport-of-intensity quantitative phase microscopy with annular illumination. *Sci. Rep.* **7**, 7654 (2017).

16. Fan, C. et al. Flexible dynamic quantitative phase imaging based on division of focal plane polarization imaging technique. *Opt. Express* **31**, 33830 (2023).

17. Picazo-Bueno, J. A. & Micó, V. Optical module for single-shot quantitative phase imaging based on the transport of intensity equation with field of view multiplexing. *Opt. Express* **29**, 39904 (2021).

18. Waller, L., Tian, L. & Barbastathis, G. Transport of Intensity imaging with higher order derivatives. *Opt. Express* **18**, 12552 (2010).

19. Jingshan, Z., Claus, R. A., Dauwels, J., Tian, L. & Waller, L. Transport of Intensity phase imaging by intensity spectrum fitting of exponentially spaced defocus planes. *Opt. Express* **22**, 10661 (2014).

20. Ghosh, K. K. et al. Miniaturized integration of a fluorescence microscope. *Nat. Methods* **8**, 871–878 (2011).

21. Shekhtmeyster, P. et al. Multiplex translaminar imaging in the spinal cord of behaving mice. *Nat. Commun.* **14**, 1427 (2023).

22. Ozcan, A. & McLeod, E. Lensless Imaging and Sensing. *Annu. Rev. Biomed. Eng.* **18**, 77–102 (2016).

23. Wu, X. et al. Wavelength-scanning lensfree on-chip microscopy for wide-field pixel-super-resolved quantitative phase imaging. *Opt. Lett.* **46**, 2023 (2021).

24. Zhang, H. et al. Field-portable quantitative lensless microscopy based on translated speckle illumination and sub-sampled ptychographic phase retrieval. *Opt. Lett.* **44**, 1976 (2019).

25. Ye, X. et al. Chip-scale metalens microscope for wide-field and depth-of-field imaging. *Adv. Photonics* **4**, 046006 (2022).

26. Xu, B. et al. Metalens-integrated compact imaging devices for wide-field microscopy. *Adv. Photonics* **2**, 066004 (2020).

27. Khorasaninejad, M. et al. Metalenses at visible wavelengths: Diffraction-limited focusing and subwavelength resolution imaging. *Science* **352**, 1190–1194 (2016).

28. Yu, N. et al. Light propagation with phase discontinuities: generalized laws of reflection and refraction. *Science* **334**, 333–337 (2011).

29. Hao, J. et al. Lensless complex amplitude demodulation based on deep learning in holographic data storage. *Opto-Electron. Adv.* **6**, 220157 (2023).

30. Zhang, F. et al. Meta-optics empowered vector visual cryptography for high security and rapid decryption. *Nat. Commun.* **14**, 1946 (2023).

31. Li, X. et al. Time-sequential color code division multiplexing holographic display with metasurface. *Opto-Electron. Adv.* **6**, 220060 (2023).

32. Zhang, F. et al. All-dielectric metasurfaces for simultaneous giant circular asymmetric transmission and wavefront shaping based on asymmetric photonic spin–orbit interactions. *Adv. Funct. Mater.* **27**, 1704295 (2017).

33. Li, T. et al. Revolutionary meta-imaging: from superlens to metalens. *Photonics Insights* **2**, R01 (2023).

34. Chen, C. et al. Bifacial-metasurface-enabled pancake metalens with polarized space folding. *Optica* **9**, 1314 (2022).

35. Arbabi, E. et al. Two-photon microscopy with a double-wavelength metasurface objective lens. *Nano Lett.* **18**, 4943–4948 (2018).

36. Luo, Y. et al. Varifocal metalens for optical sectioning fluorescence microscopy. *Nano Lett.* **21**, 5133–5142 (2021).

37. Rubin, N. A. et al. Matrix Fourier optics enables a compact full-Stokes polarization camera. *Science* **365**, eaax1839 (2019).

38. Yang, J. et al. Ultraspectral imaging based on metasurfaces with freeform shaped meta-atoms. *Laser Photon Rev.* **16**, 2100663 (2022).

39. Engay, E., Huo, D., Malureanu, R., Bunea, A. I. & Lavrinenko, A. Polarization-dependent all-dielectric metasurface for single-shot quantitative phase imaging. *Nano Lett.* **21**, 3820–3826 (2021).

40. Kwon, H., Arbabi, E., Kamali, S. M., Faraji-Dana, M. S. & Faraon, A. Single-shot quantitative phase gradient microscopy using a system of multifunctional metasurfaces. *Nat. Photonics* **14**, 109–114 (2020).

41. Wu, Q. et al. Single-shot quantitative amplitude and phase imaging based on a pair of all-dielectric metasurfaces. *Optica* **10**, 619 (2023).

42. Huo, P. et al. Photonic spin-multiplexing metasurface for switchable spiral phase contrast imaging. *Nano Lett.* **20**, 2791–2798 (2020).

43. Kim, Y., Lee, G. Y., Sung, J., Jang, J. & Lee, B. Spiral metalens for phase contrast imaging. *Adv, Funct, Mater,* **32**, 2106050 (2022).

44. Wang, X. et al. Single-shot isotropic differential interference contrast microscopy. *Nat, Commun,* **14**, 2063 (2023).

45. Zhou, J. et al. Fourier optical spin splitting microscopy. *Phys. Rev. Lett.* **129**, 020801 (2022).

46. Chen, C. et al. Spectral tomographic imaging with aplanatic metalens. *Light Sci. Appl.* **8**, 99 (2019).

47. Pahlevaninezhad, M. et al. Metasurface-based bijective illumination collection imaging provides high-resolution tomography in three dimensions. *Nat. Photonics* **16**, 203–211 (2022).

48. Ye, X. et al. Ultracompact multimode meta-microscope based on both spatial and guided-wave illumination. *Adv Devices Instrum.* **4**, 0023 (2023).

49. Chen, J. et al. Planar wide-angle-imaging camera enabled by metalens array. *Optica* **9**, 431 (2022).

50. Waller, L., Kou, S. S., Sheppard, C. J. R. & Barbastathis, G. Phase from chromatic aberrations. *Opt Express* **18**, 22817 (2010).

51. Arbabi, A. et al. Miniature optical planar camera based on a wide-angle metasurface doublet corrected for monochromatic aberrations. *Nat. Commun.* **7**, 13682 (2016).

52. Goodman, J. W. *Introduction to Fourier Optics* (Roberts and Company publishers, 2005).

53. Popescu, G. et al. Optical imaging of cell mass and growth dynamics. *Am. J. Physiol.-Cell Physiol.* **295**, C538–C544 (2008).

Acknowledgements

Author contributions

J.W., R.Y., X.Y., C.C., and T.L. conceived the idea. J.W. and R.Y. conducted the imaging experiments and completed the numerical calculations. X.X., J.J., W.S., and Z.T. helped with the calculations. X.Y. and J.W. performed the simulations and characterizations of the metalens. J.S., J.L., and C.H. fabricated the metalens and the phase resolution target. J.W., R.Y., X.Y., C.C., and T.L. wrote the manuscript. C.C., S.Z., and T.L. supervised the project. All the authors analyzed the data and discussed the results. All the authors read and approved the final manuscript.

Competing interests

The authors declare no competing interests.

Additional information

Supplementary information The online version contains

supplementary material available at
https://doi.org/10.1038/s44310-024-00007-8.

Correspondence and requests for materials should be addressed to Chen Chen or Tao Li.